Aerospace Europe Conference 2023 - 10^{th} EUCASS - 9^{th} CEAS

ID: 643

Time-Resolved Reconstruction of the Plume of a Pulsed Plasma Thruster (PPT)

Scherezade Barquero[⋆†]*, Jaume Navarro-Cavallé*[⋆] *and Mario Merino*[⋆]
[⋆]*Equipo de Propulsión Espacial y Plasmas (EP2), Universidad Carlos III de Madrid*
Leganés, Spain
[†]mbalsera@ing.uc3m.es

Abstract

The transient exhaust of an ablative Pulsed Plasma Thruster PPT is characterized experimentally at different discharge voltages, always below 8 J of energy. The time series measured by three plasma probes operated at the ion saturation regime and placed at various distances downstream from the device are fitted to a model of the discharge. This model discretizes the exhaust into separate Maxwellian ion groups. Each group is characterized by its own parameters: mean velocity, thermal spread, amplitude of the signal, time of creation, and divergence. Results show that a good fit is possible only considering three ion groups for all the explored operating points. The order of magnitude of the velocity for each group is found to be about 50, 35 and under 20 km/s. Plume current increases with the discharge energy, while the first ion group velocity slightly decreases with the discharge voltage. The thermal spread is always below 20 km/s.

Keywords*: Ablative Pulsed Plasma Thruster, PPT / APPT, transient plume, Lagmuir probes, time-of-flight (ToF), nanosatellites*

1. Introduction

Ablative Pulsed Plasma Thrusters (APPT) are electromagnetic plasma propulsion systems.[1,2] In essence, an APPT consists of a pair of parallel electrodes (cathode-anode) which shapes a channel-like configuration. On one end, the solid propellant, typically PTFE, is embedded in between the electrodes. The surface layer of this propellant is ablated[3] and ionized by applying a large cathode-anode voltage, V_0. Once the plasma is generated, the current generates a self-induced magnetic field that results in a Lorentz force, which accelerates the plasma down the channel, until it is ejected from the channel. Fig. 1 shows an ablative PPT discharge sequence to illustrate the description above.

In contrast to other plasma thrusters, this technology is suitable for low power operation (constraining the maximum pulsing frequency allowed by the power circuit) and miniaturization, which constitutes an opportunity for nanosatellites to have on-board propulsion. Nevertheless, this technology also has some drawbacks, such as electromagnetic compatibility with other subsystems,[4] or its lifetime, shorten by erosion and contamination which are difficult to be predicted.[5–8]

Since the 60s, multiple research groups have been working on systematic studies of PPTs at different energy levels. However, the efforts to describe the discharge physical mechanisms in detail have been so far limited.[12,13] Among other aspects, the nano- and microsecond characteristic time scales involved, together with the peculiarity of dealing with a multi-species pulsed plasma, stand as major difficulties. Hence, many challenges still prevail concerning the understanding of the ablative PPT discharge, the underlying physics and the influence of geometrical and operational design parameters.

The characterization of the plasma exhaust is important to further understand the discharge process, and its interaction with neighboring surfaces. The plume divergence has also a direct effect on the efficiency of the device. Relevant studies on PPT plumes provided evidence of the existence of multiple ion groups by using time-of-flight (ToF)[10,14–18] techniques. Two ion populations with mean axial velocities around 60 km/s and 30 km/s as maximum were identified for different operation regimes, even at very low energy, below 5 J. Additional spectroscopy studies[19] were able to identify multiply ionized species of carbon and fluorine atoms, relating them with the following axial speed ranges: $C^+ \sim 5-20$ km/s, $C^{2+} \sim 20-30$ km/s, $C^{3+} \sim 30-40$ km/s, $F^+ \sim 5-15$ km/s, $F^{2+} \sim 15-20$ km/s, and $F^{3+} \sim 20-30$ km/s.

In this work, the exhaust of a new APPT breadboard model, breech-fed and parallel-rail, is experimentally characterized. The data is then used to reconstruct a model of its time-varying plasma exhaust consisting of multiple

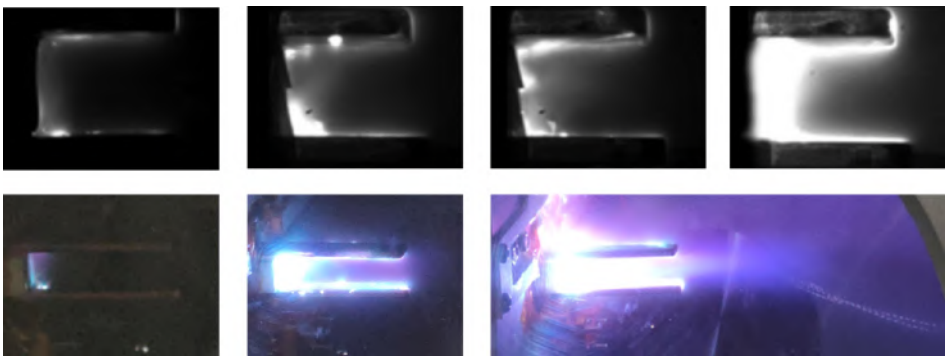

Figure 1: **Two different sequences of an APPT discharge sequences. Discharge Channel height** 1 **cm.** The discharge evolves from a plasma seed travelling towards the anode, leading to the ignition of the main channel. Canting[9] of the plasma sheet and some hot spots[10] on the electrodes are also visible. Plasma concentrates towards the electrode edges, agreeing with the deposition patterns on the electrodes reported in the literature.[11]

ion groups. A parametric study of the main capacitor bank initial voltage, V_0, from 750 to 1500 V is carried out. Fast sampled (> 100 MHz) measurements of the APPT voltage and of three plasma probes located along the plume axial axis are used.

The rest of the document is structured as follows. Section 2 presents the PPT prototype and the experimental setup. Section 3 describes the exhaust model and the fitting approach. Section 4 collects the results and corresponding discussions. After a brief analysis of the discharge waveform, it focuses on the time-varying reconstruction of the thruster exhaust. It characterizes the different ion groups involved in the plume performing the fitting on the plasma measurements. Finally, the parametric study on V_0 is addressed. Conclusions and an outlook of future work can be found in section 5.

2. Experimental setup

2.1 PPT prototype

The operation of a low-power class breech-fed and parallel-rail-electrode and flexible-to-iterate ablative PPT breadboard model and shown in Fig. 2, has been experimentally studied in this work. Its design is the result of several iterations,[11,20] and the basis of the sizing discussion can be found in a previous work.[20]

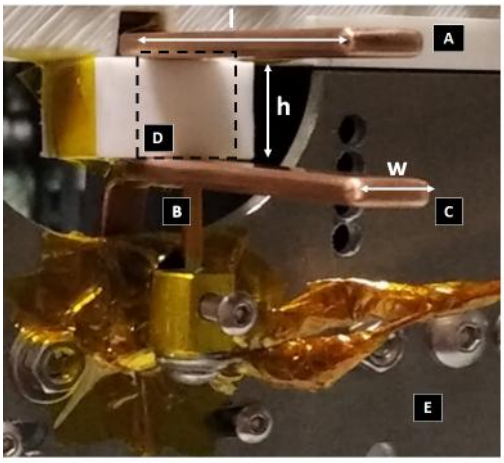

Figure 2: **Discharge channel of the ablative PPT prototype.** 'A' refers to the anode, 'C', the cathode, 'D', the effective propellant surface (PTFE), and 'E', the thruster platform which holds the discharge chamber. Concerning dimensions, l, h and w mean channel length, height and width, correspondingly.

The device features a nominal discharge chamber of 4.5 cm length (l), 1 cm height (h), 1 cm width (w), and equally-sized electrodes made of copper with the cathode grounded. A block of PTFE is used as propellant. In the rear

part of the thruster a main capacitor bank capacitance C of 6 μF is connected to the (A/C) electrodes. This capacitor bank, which is charged by a specific DC-DC converter —kept outside the chamber— to a voltage V_0 before firing, provides the electrical power to the main discharge. The firing frequency is set to 0.1 Hz to enable all the acquired data to be saved between shots.

In this work a parametric study is performed on initial main capacitor bank voltage V_0, for 750, 1000 and 1500 V. This involves 3 configurations, corresponding to discharge energies E_0 of 1.7, 3 and 6.8 J respectively. The central configuration (1000 V) is the nominal one for the device. Each study case is referenced with a number, rising up with V_0 from 1 to 3. E. g, 2 is used for the nominal case.

Once the main capacitor bank is charged up, ignition is triggered by a 1.5 kV spark plug embedded in the channel cathode electrode through a hole. This is placed close to the main propellant surface. The igniter has been developed in-house,[8,11,20] based on a Metal-Insulator-Metal (MIM) gap, with tungsten for the emitter electrode, PTFE as the dielectric filler and the cathode as the other electrode. The tungsten rod is negatively biased with respect to the cathode.

The thruster is operated inside Hedron, a 50 cm-edge cubic vacuum chamber at the EP2 laboratory. MHV feedthroughs are used to power the thruster and BNC ones for the diagnostic probes. The vacuum system of Hedron consists of a mechanical vacuum pump (Edwards nXDS Scroll pump, 10 m^3/h) and a turbomolecular pump (Edwards next400, 400 L/s (N_2)). The ultimate pressure reached is 10^{-6} mbar, perturbed at each firing by less than $2 \cdot 10^{-5}$ mbar. Pressure drops to the ultimate level in a few seconds after each firing.

2.2 Electric and plasma diagnostics

Three cylindrical Langmuir probes (LPs) with tungsten tips of 0.508 mm diameter and 3 mm length are placed along the centerline of the discharge channel as shown in Fig. 3, at distances $z_1 = 26.2$, $z_2 = 30.7$ and $z_3 = 35.0$ cm from XYZ. The LP tips are oriented perpendicularly to the plasma exhaust, and slightly displaced laterally along x so as to avoid direct shadowing among them. LPs are biased negatively to work well inside the ion saturation regime (−50 V).

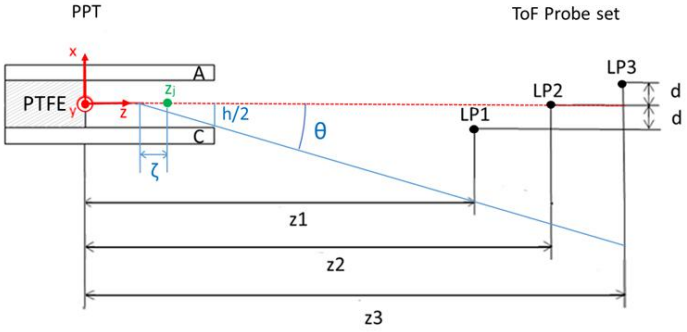

Figure 3: **Experimental setup for the time-of-flight (ToF) Langmuir probes LP placed far downstream** $z_1 = 26.2$, $z_2 = 30.7$ and $z_3 = 35.0$ cm and $d \ll z$. The schematic for the conical expansion to approach the divergence is included. 'A', anode, and 'C', cathode and h, channel height. z_j refers to the creation location of a certain ion group IG within the discharge channel. For that IG, ζ names the upstream distance between the z_j and the expansion vertex and θ is the divergence angle. Not to scale drawing.

Teledyne LeCroy high voltage passive probes were used for voltage monitoring of the triggering and main discharge batteries. An eight-channel Yokogawa DLM5000 oscilloscope is used for data acquisition from all the probes synchronously. The oscilloscope sampling frequency is set above 100 MHz.

3. Data processing method

Under the assumption that the effective collection area A_{probe} is equal and constant for the three identical ion saturation probes, the current measured by each of them as a function of time is $I_k(t) = j_i(z_k, t)A_{probe}$ $(k = 1, 2, 3)$, where j_i is the ion current density in the exhaust. Traditional ToF diagnostics estimate the ion mean velocity simply as $\bar{v} \simeq \Delta z/\Delta t$, where Δz is the distance between two probes and Δt the difference in time for peak current occurrence at the probes. Additionally, a first approach of the exhaust plume divergence rate can be carried out noting the product of the peak value of I_k and the exhaust cross-sectional area A_{plume} must be approximately equal at the two probes. So,

$\mathrm{d}\ln A_{plume}/\mathrm{d}z \simeq -\Delta \ln I_{k,peak}/\Delta z$. A preliminary work addressing the methodology above can be found in the referenced literature.[8]

However, this analysis neglects two major aspects of the plasma expansion, and may consequently incur in large error. First, the exhaust likely consists of more than one ion group (IG), potentially originating at different times, and with different mass/charge ratios, velocities, densities, thermal spreads, and divergence rates. The overlapping contributions of different IGs may result in multiple maxima in the measured current $I_\mathrm{k}(t)$, perhaps with none of them coinciding with the peak current of any individual group. Thus, that analysis can only provide an 'average' velocity and plume divergence rate of the exhaust. Second, it should be noted the ion current density j_i decreases downstream not only due to the exhaust divergence, but due to the axial thermal spread of each individual IG too. Hence, that calculation overestimates the plume divergence rate.

To overcome these limitations, it is necessary to reconstruct the parameters of the IGs from the time series data, by establishing a model of their expansion. It also offers additional insight into other characteristics mentioned above of the plasma exhaust.

For the sake of simplicity, the j-th IG is assumed to be generated as a sheet of plasma of small thickness $\delta \to 0$ about a position z_j within the discharge channel, at a discrete time t_j after the initiation of the breakdown. The population of ions of the IG is homogeneous in charge and mass, and has a Maxwellian distribution with charge density $Q_\mathrm{j}\delta(z-z_\mathrm{j})$, mean axial velocity $\bar{v}_\mathrm{j}$, and axial thermal velocity c_j:

$$f_\mathrm{j}(z, v>0) = \frac{Q_\mathrm{j}}{\sqrt{2\pi c_\mathrm{j}^2}} \frac{\exp\left[-\dfrac{(v-\bar{v}_\mathrm{j})^2}{2c_\mathrm{j}^2}\right]}{\dfrac{1}{2}\mathrm{erf}\left(\bar{v}_\mathrm{j}/\sqrt{2c_\mathrm{j}^2}\right)+1}\delta(z-z_\mathrm{j}) \equiv F_\mathrm{j}(v)\delta(z-z_\mathrm{j}). \tag{1}$$

Once the IG leaves its initial position z_j, the effect of subsequent axial ion acceleration by the ambipolar electric field is ignored. Subsequently, as the IG travels downstream, it expands axially due to its thermal spread, and laterally as a cone with vertex located at a position ζ_j upstream from z_j (see Fig. 3). The divergence half-angle of the IG is then defined as $\theta_\mathrm{j} = \arctan[h/(2\zeta_\mathrm{j})]$, where h is the distance between the channel electrodes.

Ions of the j-th IG having axial velocity v reach probe location z_k at a time $t = t_\mathrm{j} + (z_\mathrm{k} - z_\mathrm{j})/v$. Integrating over the distribution function, the contribution of this IG to the modeled ion current density at probe k is:

$$\tilde{j}_\mathrm{i}(z_\mathrm{k}, t)|_\mathrm{j} = \left[\frac{\zeta_\mathrm{j}}{(z_\mathrm{k}-z_\mathrm{j})+\zeta_\mathrm{j}}\right]^2 F_\mathrm{j}\left(\frac{z_\mathrm{k}-z_\mathrm{j}}{t-t_\mathrm{j}}\right)\frac{z_\mathrm{k}-z_\mathrm{j}}{(t-t_\mathrm{j})^2}, \tag{2}$$

Then, the modeled ion current density $\tilde{j}_\mathrm{i}(z_\mathrm{k}, t)$ measured at each probe is the sum of the contributions of all IGs,

$$\tilde{j}_\mathrm{i}(z_\mathrm{k}, t) = \sum_\mathrm{j} \tilde{j}_\mathrm{i}(z_\mathrm{k}, t)|_\mathrm{j}\,. \tag{3}$$

The normalized least square error between the model and the experimental data is

$$\varepsilon = \sum_\mathrm{k} \varepsilon_\mathrm{k} = \sum_\mathrm{k} \frac{\int \left[j_\mathrm{i}(z_\mathrm{k}, t) - \tilde{j}_\mathrm{i}(z_\mathrm{k}, t)\right]^2 \mathrm{d}t}{\int j_\mathrm{i}^2(z_\mathrm{k}, t)\mathrm{d}t}, \tag{4}$$

where the integrals span a specified time window. Note the sum of the error at each probe, ε_k, is used to define ε.

After visual inspection of the current collected by the probes and some trial and error, it was decided to use up to 3 IGs for the numerical fitting of the data. The determination of the model parameters $(Q_\mathrm{j}, \bar{v}_\mathrm{j}, c_\mathrm{j}, z_\mathrm{j}, t_\mathrm{j}, \zeta_\mathrm{j})$ for $j = 1, 2, 3$ is carried out as follows. First, $z_\mathrm{j} = 2.5$ cm is set for all three IGs —with $z = 0$ on the PTFE surface as in Fig. 3. The reminder of parameters is found by minimizing ε, along the time window spanning from 3 to 30 μs —the tail beyond that was verified not to affect the fitting—, with the following constraints. Setting $t = 0$ at the breakdown, $t_\mathrm{j} > 0$ to avoid nonphysical solutions. The mean axial speed of successive ion groups $t_{\mathrm{j}+1} > t_\mathrm{j}$ is sorted as $\bar{v}_{\mathrm{j}+1} < \bar{v}_\mathrm{j}$. In case 2 $0.5 < \zeta_{\mathrm{j}+1}/\zeta_\mathrm{j} < 2$ is applied to keep Q_j within the same order of magnitude along the 3 IGs. It has no impact on the rest of the fitting parameters.

4. Results

4.1 Discharge characterization

It is first analyzed the electrical discharge of the ablative PPT. The anode voltage $V(t)$ in the nominal case (case 2: $V_0 = 1000$ V, $C = 6$ μF) is shown in Fig. 4 (top) for multiple realizations. The common time reference for the shots

is the anode null-voltage instant, which is set to $t = 0.8\ \mu$s. The time response exhibits the characteristic underdamped oscillation with natural frequency in the order of 100 kHz before decaying to zero after 4 cycles or about 6 μs. The amplitude of those oscillations grows up with V_0.[8] The estimated R and L values from fitting a typical RCL circuit are a couple of tens of mΩ and nH respectively, roughly constant with V_0. Overall good repeatability among pulses is observed, although small differences develop after the second period the discharge.

Superimposed on this low frequency, high-frequency noise (> 10 MHz) can be observed during the breakdown instants and also in the minima of the anode voltage response. The later is not visible for the largest V_0 studied. These could be related to late re-ignitions reported in the literature.[21–23]

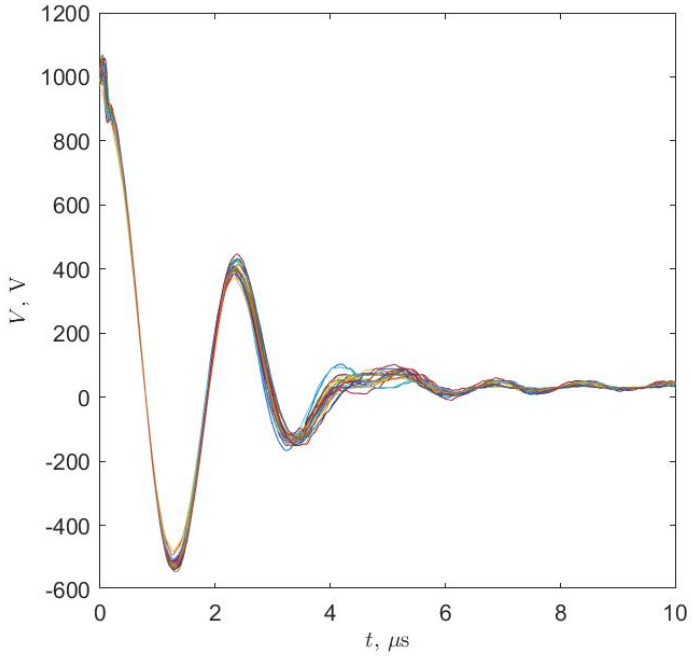

Figure 4: **Anode voltage discharge waveform measured for the nominal case (2).**

4.2 Plume characterization

Fig. 5 displays the response of I_1, the measured current at the first LP, in the nominal case. Individual firings are shown using thin lines, while the thick line indicates the mean response, to illustrate the variability among firings. In spite of the good repeatability of the voltage signal discussed in Section 4.1, probe current variability can be up to about ±25% with respect to the mean at some instants of time. Firings with abnormal current responses have been cast aside from the analysis. The retained firings represent about the 60 % of the ones carried out.

The probe begins collecting current around 4 μs after the initiation of the discharge, and the signal vanishes 30–40 μs afterward. Three peaks or bumps are clearly visible in the probe current response, which the authors identify with distinct IGs emanating from the thruster.

Fig. 6 presents the ion current model fitted to the the mean probe current, proving the overall validity of the decomposition approach. Out of the three IGs, the first two are large, concentrated peaks that occur at early times, and together contribute to the peak value of I_1. The third IG arrives later at the probe, and has a smaller but broader contribution.

The fitting parameters of the 3 IGs for the nominal case are shown in Table 1. Indeed, the first two IGs originate roughly at the same time. The first one has larger density and mean velocity (Q_j and $\bar{v}_j$) than the second, but also larger thermal spread (represented by c_j) and divergence (i.e., lower ζ_j). The third IG would originate at a later time, with smaller density but similar mean velocity than the IG2, and a smaller divergence.

The relative integral error $\sqrt{\varepsilon}$ does not distribute homogeneously among the three probes. Indeed, probe number 3 incurs in a larger error than the other two. Nevertheless, the disagreement with the measurements is less than 10 % in each of them in the nominal case —less than 5 % for probes 1 and 2.

4.2.1 Parametric analysis

The current at the three probes is shown in Fig. 1 for the 3 tested cases as a function of the initial discharge voltage V_0 (750, 1000 and 1500 V). Each panel plots the mean current and the standard deviation over multiple measurements,

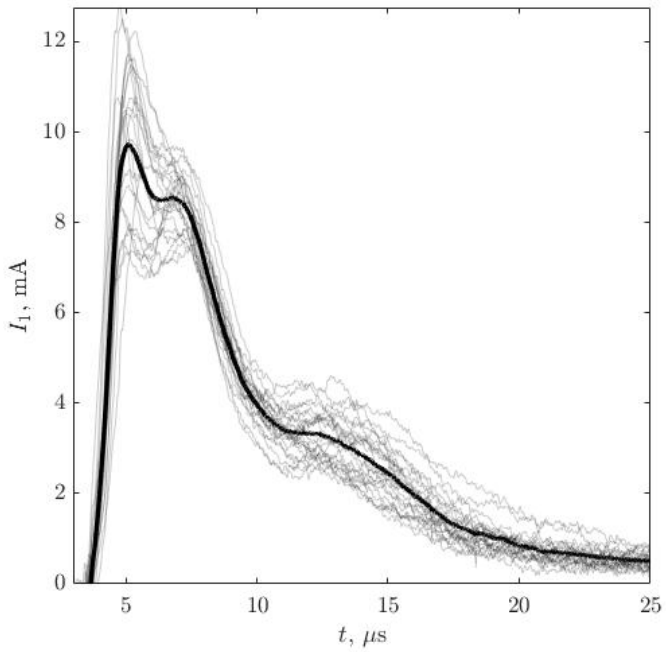

Figure 5: **Ion saturation current measured at LP** 1**,** I_1**, for the nominal case (2)**. Thin lines are individual firings, whilst the thick one is their mean.

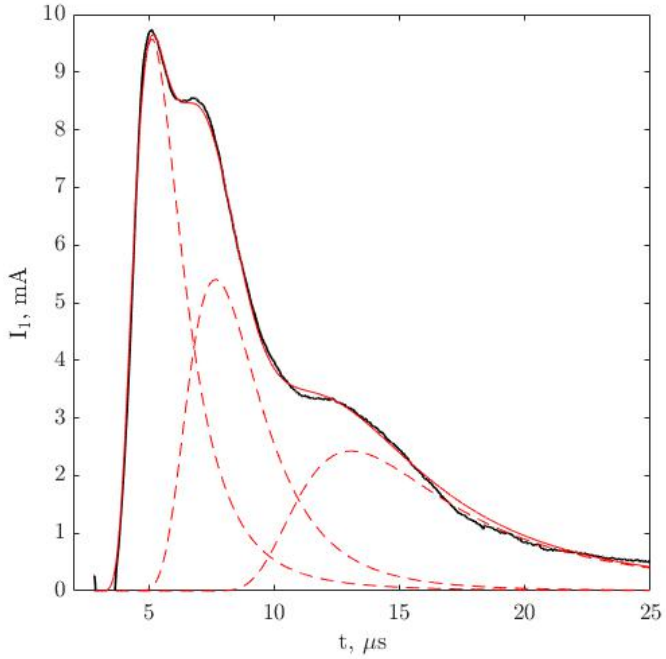

Figure 6: **Ion saturation current measured at LP** 1**,** I_1**, for the nominal case (2), distinguishing the ion groups, IGs, contributing**. Black line shows the mean measured probe current; red dashed lines show the contributions of the three IGs in the model; the solid red line is the sum of them.

and the fitted model for each case. The fitting parameters of the IGs are reported in Table 1.

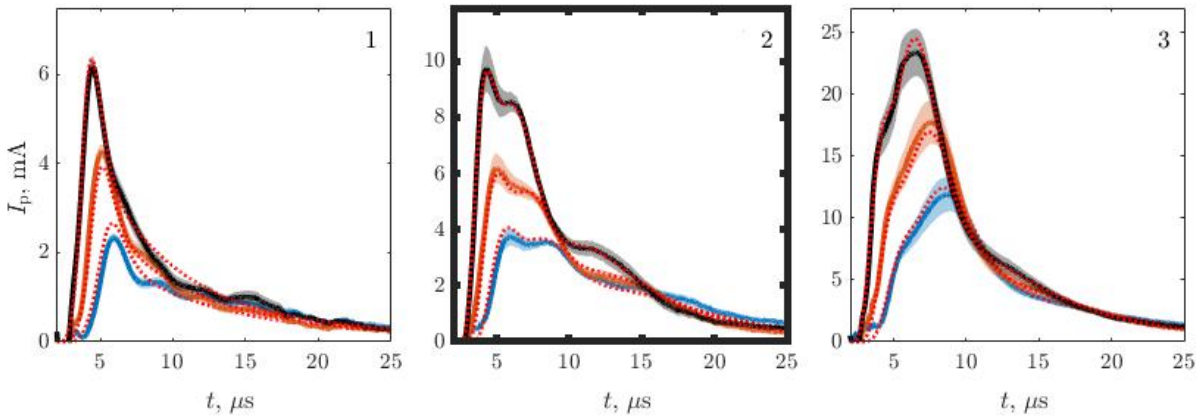

Figure 1: **Mean ion saturation current over multiple measurements by the set of LPs and the fitted model for each V_0 case.** LP 1 results, I_1, in black, LP 2, I_2, in blue and LP 3, I_3, in red. The mean is represented by the continuous thick line with the standard deviation shaded, while the fitting corresponds to the dot red line. Note the different y-axis scale in each subplot

.

Some general trends can be observed. Firstly, current is mainly driven by the first IGs, and the relative importance gained by the second IG with V_0 in the graphs, with respect to the first IG increases. At the same time, the shape of the current curves becomes more complex. There is partial evidence of additional IGs in the tail of the discharge, e.g. in 1. Although using a larger number of IGs (and therefore larger number of degrees of freedom) would yield a lower error, it is found that the extra complexity does not provide much additional physical insight, and moreover, can result in an overfitted model susceptible to capture experimental noise and error.

Second, the accumulated current recorded by each probe along the collecting time, as well as its maxima, across all the three cases are seen to proportionally scale with the discharge energy $E_0 = CV_0^2/2$ as depicted in Fig. 2. These trends are not evident from the Q_j parameter for each IG alone, shown in Table 1, as the peak values of each IG at the three probes depend not only on Q_j but also on $\bar{v}_j$, c_j, and ζ_j. A linear trend for the impulse bit with E_0 was also reported for an electrothermal PPT,[24] through direct thrust measurements.

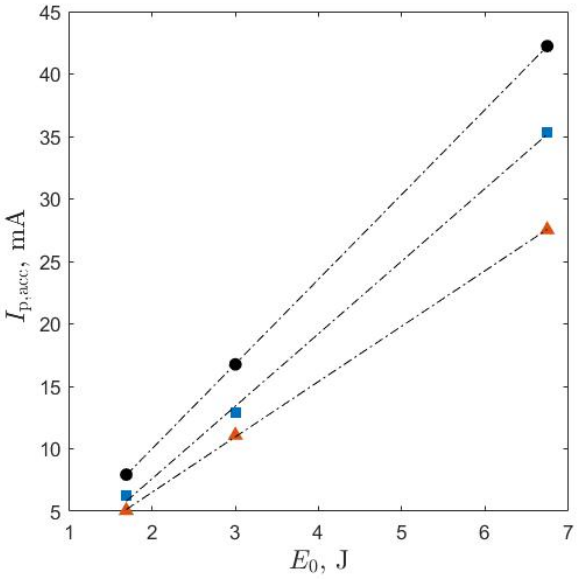

Figure 2: **Accumulated mean ion saturation current as a function of the discharge energy E_0.** Probe 1 in black, I_1, probe 2 in blue, I_2, and probe 3 in red, I_3.

Table 1: **Fitting parameters of each V_0 case.**

Case	V_0 V	C μF	E_0 J	IG_j	t_j μs	$Q_j A_{probe}$ C	$\bar{v}_j$ km/s	c_j km/s	ζ_j cm	$\sqrt{\epsilon_1}$	$\sqrt{\epsilon_2}$ %	$\sqrt{\epsilon_3}$
1	750	6	1.7	1	1.33	0.70	59	10	2.3	8.4	8.2	18.8
				2	1.54	0.82	35	28	4.2			
				3	1.85	0.30	5.0	20	7.2			
2	1000	6	3	1	1.30	1.34	54	16	3.9	2.9	5.1	9.1
				2	1.30	0.36	33	9.0	7.9			
				3	3.64	0.16	19	9.0	15.7			
3	1500	6	6.8	1	0.83	0.69	42	16	11.9	2.7	5.3	5.2
				2	1.82	0.39	35	1.0	16.7			
				3	2.12	0.41	15	6.0	11.3			

Third, IG mean velocity $\bar{v}_j$ of IG1 slightly decreases with V_0, while for IG2 keeps being roughly the same and for the third increases. The thermal velocity c_j does not follow a clear trend, other than being often decreasing form IG1 to IG2 to IG3. Values of $\bar{v}$ are in the range of those the reported by other authors, such as A. Solbes et al.[14] or N. Gatsonis and others.[16] The majority of values of c_j fall under 20 km/s.

Fifth, overall ζ_j keeps rising with V_0, as well as along the IGs. It suggests a lower plume divergence angle at higher energies and for the later the IG is generated.

Finally, the relative integral error $\sqrt{\varepsilon_k}$ at each probe remains in most cases under about 10 %. As in the central case, the largest misfits occur at the third probe, farther downstream than the others and therefore in a region of lower density. Possibly, measurements at this probe are also affected by the wakes of the other two.

5. Conclusions

The discharge of a small ablative pulsed plasma thruster prototype has been experimentally characterized for three discharge voltages V_0. After briefly introducing the discharge characterization, the study focuses on the plume. The plume exhaust is reconstructed by means of an original reinterpretation of the time of flight technique. The proposed model provides an estimate of the upstream velocity distribution (characteristic velocity and thermal spread of each of the ion groups, as well as their magnitude, time of creation) and divergence of the different ion groups involved from the measurements collected by the Langmuir probe arrangement located downstream. The fitted results reveal that three ion populations suffice overall to explain the explored operation cases. Successively generated, each ion group is assumed travelling at constant mean speed across the plume at about 50, 35 and under 20 km/s respectively. Increasing the discharge energy ($E_0 = CV_0^2/2$), it is evidenced that the mean speed of the first ion group slightly decreases but that a larger plume current develops. Plume current is mainly driven by the first ion groups and the data suggest it linearly scales with the discharge energy. As well as the relative weight of the second ion group grows up faster than the others with voltage increments.

Less clear trends were obtained for the thermal spread and the divergence. The thermal spread usually keeps under 20 km/s and often decreases from an ion group to the next one. Overview findings regarding the divergence show a confined exhaust with an estimated $\theta < 10°$, typically lowering for the further ion groups and for the higher the V_0 is.

While Fig. 6 shows that the model used in this work can accurately describe the ions in the PPT exhaust, it is worth identifying its possible main drawbacks and limitations. Firstly, it is observed that the free parameters that describe each ion group are not "orthogonal" to each other in the optimization process. That is, if one models the integral error ε as a paraboloid around its minimum, the free parameters do not represent its principal directions. This translates into that the relative uncertainty of the value of each parameter is not the same. Secondly, the effect of experimental error in each one of the probes. This deals with the uncertainty regarding working with the mean firing, and especially with slight differences in the probe geometry and axial alignment. As the fitting behaves worse for probes located farther downstream, this may suggest the model still has room for improvement. Thirdly, the main inherent limitations of the model are as follows. The initial volume and creation interval of each IG are ignored under the assumption that $\delta/z_p \ll 1$, $t_j\bar{v}_j/z_p \ll 1$. And, the effect of Lorentz forces and collisions on the evolution of the IGs is neglected.

Concerning the divergence angle, highly focused plume results probably indicate underestimated ion group divergence. Hence, improving the expansion model to not only consider axial measurements, will allow non-uniform

current distributions along the cross axes, expected at least to fade with the radial distance. Indeed, in a preliminary work[8] introducing a novel probe-grid diagnostic system to characterize the plume cross section, reported measurements also suggested a bi-mode current distribution and $> 20^{\circ}$ of divergence. As a consequence, next steps will require the systematic experimental study of the time-resolved plume profile along the two cross directions, for different operation conditions and channel geometries.

6. Acknowledgments

This work was been supported by the MARTINLARA project, funded by the Comunidad de Madrid, under Grant reference P2018/NMT-4333 MARTINLARA-CM.

Additional support came from the ESPEOS project, funded by the Agencia Estatal de Investigación (Spanish National Research Agency), under Grant number PID2019-108034RB-I00/AEI/10.13039/501100011033.

References

[1] Jahn, R., *Physics of Electric Propulsion*, Dover, 2006.

[2] Burton, R. and Turchi, P., "Pulsed plasma thruster," *J. Propulsion and Power*, Vol. 14, 1998, pp. 716–735.

[3] Miller, H. C., "Surface flashover of insulators," *IEEE transactions on electrical insulation*, Vol. 24, No. 5, 1989, pp. 765–786.

[4] Hoskins, W. A., Rayburn, C., and Sarmiento, C. J., "PULSED PLASMA THRUSTER ELECTROMAGNETIC COMPATIBILITY: HISTORY, THEORY, AND THE FLIGHT VALIDATION ON EO-1," 2003.

[5] Shaw, P. and Lappas, V., "Modeling of a pulsed plasma thruster; simple design, complex matter," *Space Propulsion Conference*, 2010.

[6] Wu, Z., Sun, G., Yuan, S., Huang, T., Liu, X., Xie, K., and Wang, N., "Discharge reliability in ablative pulsed plasma thrusters," *Acta Astronautica*, Vol. 137, 2017, pp. 8–14.

[7] Sun, G. and Wu, Z., "Ignition mechanism in ablative pulsed plasma thrusters with coaxial semiconductor spark plugs," *Acta Astronautica*, Vol. 151, 2018, pp. 120–124.

[8] Barquero, S., Merino, M., and Navarro-Cavallé, J., "Experimental plume characterization of a low-power Ablative Pulsed Plasma Thruster (APPT)," 37^{th} *International Electric Propulsion Conference*, No. IEPC-2022-556, Electric Rocket Propulsion Society, Boston, MA, June 19-23, 2022.

[9] Markusic, T. E., Berkery, J. W., and Choueiri, E. Y., "Visualization of current sheet evolution in a pulsed plasma accelerator," *IEEE Transactions on Plasma Science*, Vol. 33, No. 2, 2005, pp. 528–529.

[10] Ling, W., Zhang, Z., and Tang, H., "Progress in Fundamental Pulsed Plasma Thruster Research," *35th International Electric Propulsion Conference, Electric Rocket Propulsion Soc., IEPC Paper*, Vol. 140, 2017.

[11] Barquero, S., Merino, M., and Navarro-Cavallé, J., "Preliminary test campaign of an ablative pulsed plasma thruster for micropropulsion," 5^{th} *International Workshop on Micropropulsion and CubeSats*, Toulouse (online), 2021.

[12] Ling, W. Y. L., Schönherr, T., and Koizumi, H., "Characteristics of a non-volatile liquid propellant in liquid-fed ablative pulsed plasma thrusters," *Journal of Applied Physics*, Vol. 121, No. 7, 2017, pp. 073301.

[13] Zhao, Y. and Wu, J., "A review on plasma diagnosis technology of pulsed plasma thruster," *Journal of Physics: Conference Series*, Vol. 1952, IOP Publishing, 2021, p. 032087.

[14] SOLBES, A., Thomassen, K., and VONDRA, R. J., "Analysis of solid teflon pulsed plasma thruster," *Journal of Spacecraft and Rockets*, Vol. 7, No. 12, 1970, pp. 1402–1406.

[15] Myers, R., Arrington, L., Pencil, E., Carter, J., Heminger, J., and Gatsonis, N., "Pulsed plasma thruster contamination," *32nd joint propulsion conference and exhibit*, 1996, p. 2729.

[16] Gatsonis, N. A., Eckman, R., Yin, X., Pencil, E. J., and Myers, R. M., "Experimental investigations and numerical modeling of pulsed plasma thruster plumes," *Journal of Spacecraft and Rockets*, Vol. 38, No. 3, 2001, pp. 454–464.

[17] Gatsonis, N. A., Byrne, L. T., Zwahlen, J. C., Pencil, E. J., and Kamhawi, H., "Current-mode triple and quadruple Langmuir probe methods with applications to flowing pulsed plasmas," *IEEE transactions on plasma science*, Vol. 32, No. 5, 2004, pp. 2118–2129.

[18] Pellegrini, G., Mancini, E., Paganucci, F., and Andrenucci, M., "Development and Characterization of a Pulsed Plasma Thruster," *Space Propulsion 2018*, 2018.

[19] Thomassen, K. I. and Vondra, R. J., "Exhaust velocity studies of a solid Teflon pulsed plasma thruster," *Journal of Spacecraft and Rockets*, Vol. 9, No. 1, 1972, pp. 61–64.

[20] Barquero, S., Merino, M., and Navarro-Cavallé, J., "Design of an experimental ablative pulsed plasma thruster for micropropulsion," *Space Propulsion Conference 2021*, No. 00254, Association Aéronautique et Astronautique de France, March 17-19, 2021.

[21] Koizumi, H., Noji, R., Komurasaki, K., and Arakawa, Y., "Plasma acceleration processes in an ablative pulsed plasma thruster," *Physics of plasmas*, Vol. 14, No. 3, 2007.

[22] Ziemba, T., Winglee, R., and Euripides, P., "Parameterization of the Laboratory Performance of the Mini-Magnetospheric Plasma Propulsion (M2P2) Prototype," *2001, 27th International Electric Propulsion Conference*, 2001, pp. 15–19.

[23] O'Reilly, D., Herdrich, G., Schäfer, F., Montag, C., Worden, S. P., Meaney, P., and Kavanagh, D. F., "A Coaxial Pulsed Plasma Thruster Model with Efficient Flyback Converter Approaches for Small Satellites," *Aerospace*, Vol. 10, No. 6, 2023, pp. 540.

[24] Edamitsu, T. and Tahara, H., "Experimental and numerical study of an electrothermal pulsed plasma thruster for small satellites," *Vacuum*, Vol. 80, No. 11-12, 2006, pp. 1223–1228.